MDPI

Article

Fiber-Reinforced Coal Gangue-Based Alumina Aerogel Composites with Highly Thermal Stability by Ambient Pressure Drying

Kai Bo [1,2], Hongwei Liu [1,2], Yanlan Zhang [1,2] and Yongzhen Wang [1,2,*]

1   College of Materials Science and Engineering, Taiyuan University of Technology, Taiyuan 030024, China;
    bokai5054@136.com (K.B.); liuhongwei20220713@163.com (H.L.); zhangyanlan@tyut.edu.cn (Y.Z.)
2   Shanxi Joint Laboratory of Coal Based Solid Waste Resource Utilization and Green Development,
    Taiyuan 030024, China
*   Correspondence: wangyongzhen@tyut.edu.cn

Abstract: An aluminum silicate fiber/alumina aerogel (ASF/AA) composite was prepared via the sol-gel method and atmospheric drying (APD) method using coal gangue (CG) solid waste from Xingxian county, Shanxi Province, as the aluminum source. Utilizing N_2 adsorption, scanning electron microscopy, Fourier transform infrared spectroscopy, X-ray diffraction, and thermal conductivity meters, researchers examined the microstructure, composition, pore structure, and thermal insulation performance of ASF/AA composites. The thermal conductivity mechanism of the composite was analyzed. The experimental results show that most of the aluminum in CG is used. More importantly, in the process of aerogel synthesis, the atmospheric pressure drying method is used to obtain similar properties to supercritical drying. The composite material exhibits a low thermal conductivity of 0.047 W/(m·K), a high specific surface area of 416 m^2/g, and a low density of 0.26 g/cm^3 at room temperature. After heating at 1200 °C for 2 h, the thermal conductivity was as low as 0.071 W/(m·K). This strategy can not only effectively achieve a reduction in the harmfulness of solid waste coal gangue, but also alleviate the shortage of related energy and resources in our country.

Keywords: coal gangue; nanomaterials; Al_2O_3 aerogel; atmospheric pressure drying; fiber reinforcement; thermal stability

1. Introduction

Coal gangue (CG) is low-carbon rock associated with coal mining and is often discharged as solid waste. CG accounts for 10–20% of the original coal output and is the largest industrial waste in China. About 4 billion tons of CG has been stored in China over time [1–4]. A large number of piles of coal gangue not only occupy abundant land resources, but are also prone to spontaneous combustion release such as SO_2, NO_x, and other toxic and harmful gases, through infiltration pollution of groundwater and soil, causing serious damage to the environment [5,6]. Therefore, using coal gangue as a resource is of great importance with regards to environmental protection, the utilization of waste resources and the sustainable development of society. At present, the utilization of CG in China is not high; the treatment of CG is mainly focused on basic applications, such as the production of building materials and extraction of chemical products, and agricultural applications [6–11]. Realizing the resource utilization of solid waste CG is an important direction for comprehensive technical utilization of CG [7–9]. In addition to achieving green development in the coal industry, efficient coal gangue treatment and utilization can also result in the recycling of secondary resources.

Aerogel is a kind of light porous solid material composed of nano-sized particles, which exhibit low density, high specific surface area, high porosity, and low thermal conductivity [10–14]. The fabrication process is typically achieved through the utilization of sol-gel and supercritical fluid drying (SCFD) methods, with the use of aluminum alkoxide [15], organic aluminum salts [16–18], or boehmites [19,20] as precursors. The SCFD

method makes the solvent reach a critical point and form supercritical fluid by controlling the pressure and temperature. At this time, the gas–liquid phase interface disappears, the surface tension also disappears, and the skeleton structure will not be damaged during the process of fluid expulsion from the gel [21]. Because the nanoporous network structure increases the solid heat transfer path, the existence of a large number of mesoporous pores limits the movement of internal gas, thus effectively reducing the influence of solid heat transfer, gas heat transfer, and heat convection; aerogel has great potential in the field of thermal insulation. At present, the search for high-temperature resistant aerogel insulation composites is the main direction of international research [22]. However, alumina aerogels have poor mechanical qualities similar to other aerogels, making direct application in the field of thermal insulation challenging [10]. Therefore, the use of fiber-reinforced alumina aerogel is an important method to improve the mechanical properties of alumina aerogel [23,24]. C.Y. Kim [25] synthesized a flexible aerogel-glass fiber. They found that compared to pure aerogel, the composite material's mechanical qualities were noticeably better. Zhang Rubing et al. [26] reported a porous mullite zirconia fiber/Al_2O_3-SiO_2 aerogel composite. The aerogel is filled in the void of the fiber, and there is a good interface combination between the two. The composite material exhibits certain compressive strength. However, with the increase in fiber bulk density, the strength of the composite decreases gradually. Zhu Zhaoxian et al. [27] prepared Al_2O_3-SiO_2 aerogel composites with a density of 0.21–0.24 g/cm^3 using mullite fiber felt as the reinforced phase. Fiber felt plays a supporting role so that the composite material has a high bending strength (0.62–1.26 MPa). However, the production of aerogel is limited due to expensive precursors and complex processing processes [11]. Therefore, search for an inexpensive material to synthesize alumina aerogel is very much needed. Utilizing CG to create aluminum-based aerogel material has the potential to significantly lessen and render harmless the solid waste coal gangue, as well as ease the nation's energy and resource shortage [8]. This has far-reaching implications for the development of a resource-conscious society, in keeping with the modern industrial development concept. In addition to enabling the coal industry to develop sustainably, effective handling and utilization of CG can also facilitate the recycling of secondary resources.

In addition, the drying method is a key step in the synthesis of aerogels. The commonly used supercritical drying has the disadvantages of complicated process operation, high cost, and high risk. To overcome these shortcomings, alternative methods have been explored, such as atmospheric drying (APD) [28]. Atmospheric drying is a method of evaporation of liquid phase in a material by heating under atmospheric pressure conditions. It usually uses constant temperature drying ovens as drying equipment [29]. Shewale, P. M. et al. modified the silica gel surface with trimethylchlorosilane (TMCS) prior to APD, achieving a 4% volume shrinkage [30]. APD has been widely developed and matured, but it is seldom used in the preparation of fiber aerogel composites.

In the current work, using CG as raw material, thermal insulation aluminum silicate fiber/alumina aerogel composites were prepared via high-temperature calcination, acid leaching, sol-gel, and atmospheric pressure drying. This composite material has the characteristics of being lightweight and porous and having low thermal conductivity. Its thermal stability was analyzed.

2. Experimental Procedures

The schematic representation of the alumina silicate fiber/Al_2O_3 aerogel (ASF/AA) composite is shown in Figure 1. After the reaction between hydrochloric acid and coal gangue, aluminum ions are obtained. Under the action of ethanol and water, alumina sol is formed, which combines with ASF to obtain composite material sol. After gel, composite gel is obtained, and after modification, ASF/AA is prepared through APD. Simply put, the aluminum source of the composite aerogel material comes from CG.
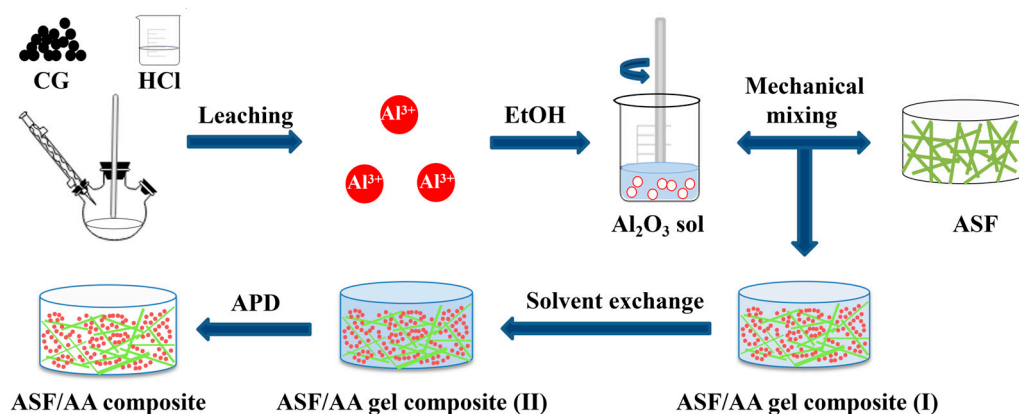
Figure 1. Schematic representation of ASF/AA composite.

2.1. Materials and Methods

The Coal gangue (CG) is from Xingxian County, Lvliang. Hydrochloric acid (HCl) was purchased from Komew Chemical Reagent Co., Ltd., (Tianjin, China). Aluminum silicate fibers (ASFs) were obtained from Yongkuo Technology Co., Ltd., (Tianmen, China). Anhydrous ethanol (EtOH), 1,2-epoxypropane (Po) and Ethylorthosilicate (TEOS) were purchased from McLean Biochemical Co., Ltd., (Shanghai, China). All reagents are analytical grade and are utilized straight out of the container without additional purification, and all experiments used deionized water (H_2O).

2.2. Preparation of AlCl₃ Precursor

The CG was sieved to 200 mesh, and then heated up at a rate of 5 °C/min in a high-temperature box resistance furnace (KSL-1200X-M of Hefei Science and Technology Materials Technology Co., Ltd., Hefei, China) to 700–900 °C, with a holding time of 0.5–3 h. After calcination, it was left standing to cool naturally. The solid–liquid ratio of CG to HCl (6 mol/L) was 1:6. It was stirred at 120 °C for 3 h. The reactions that occurred are as follows:

$$Al_2Si_2O_5(OH)_4 + 6HCl = 2AlCl_3 + 2SiO_2 + 5H_2O \tag{1}$$
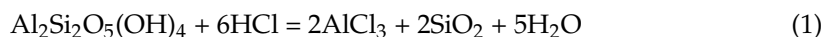
After acid leaching, the upper liquid phase was separated via centrifugation. $AlCl_3$ precursor was obtained.

2.3. Preparation of Aluminum Silicate Fiber/Al₂O₃ Aerogel

Aluminum silicate were immersed in HCl solution for several minutes and then washed with ethanol to remove impurities from their surface. Al_2O_3 sol was prepared from aluminum chloride precursor, EtOH, and H_2O at a molar ratio of $AlCl_3$:EtOH:H_2O of 1:16:10. After hydrolysis at 60 °C for 2 h, the Al_2O_3 sol was obtained. Al_2O_3 sol and ASF were placed in a dispersion stirrer and stirred at a speed of 2000 r/min to obtain aluminum sol containing ASF. Then, Po was slowly added as the gelation promoter to polymerize the sol, and the molar ratio of $AlCl_3$ to Po was 1:9. This was left to stand for gelation, which usually occurs within 0.5 h [10,31]. The aged gel was then washed with distilled water until the production color was transformed from yellow to none, which indicated that $FeCl_3$ was removed from the gel. The gel was soaked with EtOH of a quantity of twice the volume of the gel, and it was aged for 24 h at 60 °C. The wet aluminum silicate fiber/Al_2O_3 gel was immersed in a modified solvent. The modified solvent was anhydrous ethanol containing 80% tetraethyl orthosilicate, and it was soaked at 60 °C for 48 h. After modification it was exchanged with anhydrous ethanol twice at 60 °C for 12 h each time to remove impurities Cl^-, residual organic matter, and H_2O molecules. Finally, the ASF/AA composite was obtained by drying the wet aluminum silicate fiber/Al_2O_3 gel under ambient pressure at 60 °C for 6 h, 80 °C for 6 h, 100 °C for 8 h, and 120 °C for 8 h. In order to test the thermal conductivity, 10 identical samples were prepared and divided into 5 groups. One group

was not subjected to heat treatment, while the other four groups were heated to 600, 800, 1000, and 1200 °C in an air atmosphere at a heating rate of 5 °C/min, and kept warm for 2 h.

2.4. Properties and Characterizations

ASF/AA and CG were distinguished via different detection techniques. An inductively coupled plasma emission spectrometer (ICP-OES, PerkinElmer-Avio 500, Waltham, MA, USA) was used to measure the amount of iron and aluminum in the acid leaching supernatant. An AXS D8 ADVANCE (Bruker, Ettlingen, Germany) X-ray polycrystalline diffractometer (XRD) was used to determine the phase of CG and solid phase products in investigations were examined by an X-ray diffractometer (D2 phaser, Bruker, Ettlingen, Germany). ASF/AA volume density $\rho = M/V$ is the formula used to compute this based on the mass (M) and volume (V) of a single sample. The formula for calculating the ASF/AA volume shrinkage rate (V_0) is $V_0 = (V_a - V_b)/V_a$, where V_a and V_b represent the sample's pre- and post-heat treatment products, respectively. These data are the average values after three tests. Transmission electron microscopy (TEM, JEOL-200CX, JEOL, Tokyo, Japan) and scanning electron microscopy (SEM, Hitachi Regulus 8100, Hitachi, Tokyo, Japan) were used to examine the microstructure of ASF/AA both before and after heat treatment. Using a Fourier transform infrared spectrometer (FTIR, Thermo Scientific Nicolet iS20, Waltham, MA, USA), the functional groups of ASF/AA were examined. An N_2 adsorption apparatus (Micromeritics ASAP 2020 PLUS HD88, Norcross, GA, USA) was used to produce the N_2 adsorption–desorption isotherms, and Barrett Joyner Helenda (BJH) and Brunauer Emmett Teller (BET) were used to determine the samples' surface area, pore volume, and pore size. Equipped with a synchronous thermal analyzer (Netzsch Sta 449C, NETZSCH AG, Selb, Germany), the sample's thermal stability was examined. With an X-ray diffractometer, the sample's crystal structure was determined. Using a Hot Disk TPS 2500S, the thermal conductivity of ASF/AA was determined.

3. Results and Discussion

3.1. Microstructure and Properties of Coal Gangue

The chemical composition of CG is shown in Table 1. The content of Al_2O_3 in CG is very high, reaching 35%, and the SiO_2 content is 51.72%. It can also be added to concrete to improve its performance [32]. The firing vector of CG is the mass reduction caused by volatilization or decomposition of some components of coal gangue (such as carbon, oxide and non-oxide) under high-temperature conditions. The burning vector of coal gangue used in this experiment is 12.01% [33]. The XRD pattern (Figure 2a) shows that the main phases of CG samples are quartz and kaolinite. The diffraction peaks around 12.26°, 24.81°, and 20.23° of 2θ are clay mineral kaolin ($Al_2Si_2O_5(OH)_4$). The diffraction peaks around 20.99°, 26.71°, and 50.66° of 2θ correspond to the quartz phase [34]. There are many small and sharp diffraction peaks on the XRD spectrum, indicating that the phase composition of coal gangue is complex, but the overall structure is relatively stable. After calcination at high temperatures, the lattice of kaolinite in the original coal gangue sample is damaged, and the intensity of diffraction peaks is significantly reduced. the crystal structure of coal gangue changes, and kaolinite is transformed into metakaolinite. Metakaolinite has high activity, and the aluminum in it is easily dissolved [35].

Table 1. Chemical composition of Xingxian Coal gangue (wt.%).

Composition	SiO$_2$	Al$_2$O$_3$	Fe$_2$O$_3$	CaO	TiO$_2$	K$_2$O	Na$_2$O	F *
Precent (%)	51.72	35.66	4.45	2.59	2.11	1.25	0.13	12.01

* Firing vector of CG.

The above analysis shows that CG can be used as raw material for preparing aerogel. In order to fully extract aluminum from CG, it is necessary to calcinate CG at high temperatures. The calcined coal gangue reacts with HCl at 120 °C, and the insoluble material

is filtered after the reaction. ICP-OES is used to determine the content of aluminum in insoluble substances and quantify the extraction rate of aluminum. The calculation formula for the aluminum-extraction rate of CG is as follows:

$$\text{Dissolution rate}(\%) = \left(1 - \frac{m_2}{m_1}\right) \times 100 \tag{2}$$

where m_1 is the aluminum content of CG and m_2 is the aluminum content of filter residue after acid dissolution.
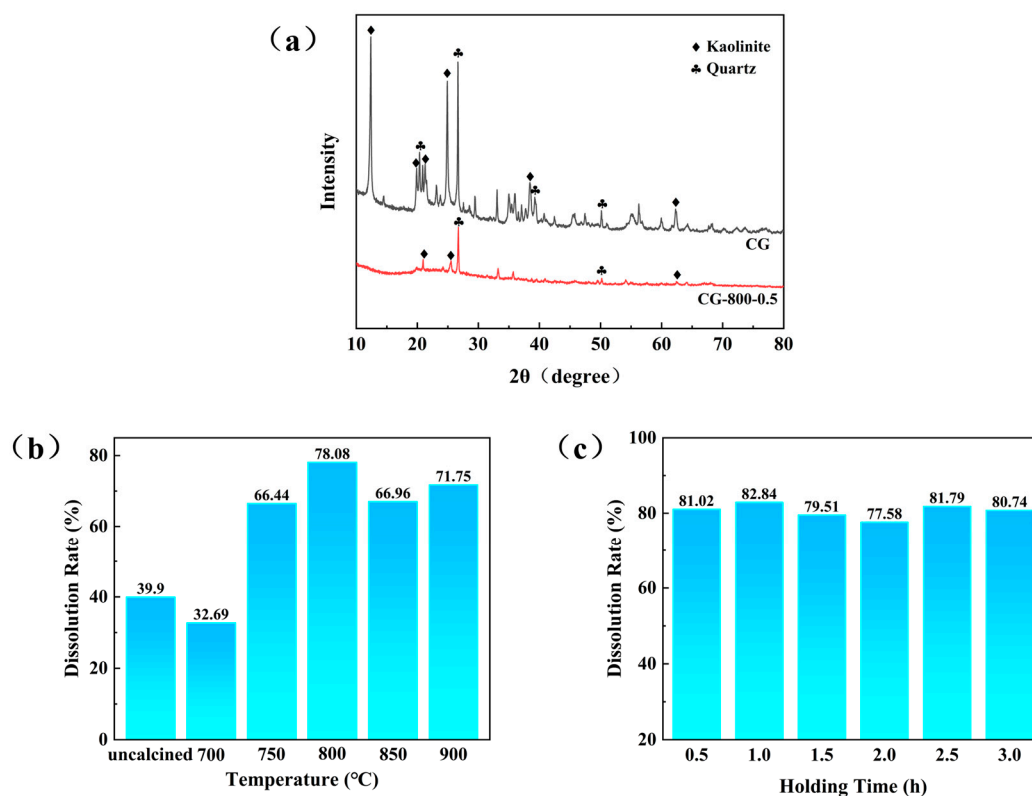

Figure 2. (**a**) XRD pattern of CG before and after calcination at the optimal temperature; (**b**) alumina-dissolution rate of CG with different temperatures; (**c**) alumina-dissolution rate of CG with different holding times.

3.2. Effects of Various Parameters on Alumina-Dissolution Rate of Coal Gangue

Two experimental parameters, including calcination temperature and holding time, are investigated in order to achieve the high dissolving rate of CG. The composition of CG before and after calcination was compared, and it was found that the crystal structure of CG would change after high-temperature calcination. The main mineral of CG is kaolinite, the ideal temperature range is 700–900 °C, too much higher will result in the formation of the mullite phase.

3.2.1. Effect of Temperature on Alumina-Dissolution Rate of Coal Gangue

The CG was calcined for 2 h at various temperatures of 700, 750, 800, 850, and 900 °C. Acid dissolution was carried out after calcination, the solid–liquid ratio of fixed CG to hydrochloric acid is 1:6. As can be seen from Figure 2b, the dissolution rate of unactivated CG is 39.9%. As the temperature rises, the dissolution rate of aluminum also rises, and when the temperature is 800 °C, it could gain a higher dissolution rate of 78.08%. This is because, within the temperature range of 700–900 °C, kaolinite in coal gangue transforms into amorphous metakaolinite, causing Al-O bond breakage, resulting in a large number of

activation points and significantly increasing the activity of kaolinite, leading to an increase in aluminum-leaching rate [36].

3.2.2. Effect of Holding Time on Alumina-Dissolution Rate of Coal Gangue

In addition, the holding time was studied. The holding times were 0.5, 1, 1.5, 2, 2.5, and 3 h at 800 °C respectively. Acid dissolution was carried out after calcination, and dissolution conditions were the same as above. The calculated results are presented in Figure 2c, which shows the influence of the holding time factor on the aluminum-extraction rate of CG, where the aluminum-dissolving rate is both high and consistent. For the purpose of energy saving, 0.5 h was selected as the holding time.

In summary, the optimized conditions for the highest dissolution rate of CG are as follows: calcination temperature of 800 °C and 0.5 h holding. Al_2O_3 in CG was extracted at a rate of 81.02% under these conditions.

3.3. Microstructure and Properties of Aluminum Silicate Fiber/Al_2O_3 Aerogel

The microstructure of ASF/AA without heat treatment is shown in Figure 3a–f. As can be seen from the macroscopic picture in Figure 3a, ASF/AA is relatively intact, with no significant surface cracking. Figure 3b is an electron microscope scan image of a single bundle of fibers after pickling. The surface is smooth and devoid of imperfections, as can be seen. Figure 3c exhibits the internal structure of ASF/AA composites. The aluminum silicate fibers are disordered in the aerogel, acting as a support skeleton, while the large pores between the fibers are filled by the Al_2O_3 aerogel with mesoporous pores, and the surface of aluminum silicate fiber is coated with a layer of aerogel, which indicates that the method of high-speed mechanical agitation assisted in thoroughly mixing alumina sol with fibers; a uniform composite sol was obtained (Figure 3d). At the same time, micrometer gaps are visible between the aluminum aerogel (AA) and fibers. In the drying process of gel, aerogel will shrink to some extent. The aerogel will be broken and cracked. The aerogel combined with the fiber may be separated, resulting in gaps between the aerogel and the fiber, and eventually forming micron-sized pores [37]. Additionally, Mizushima et al. [38] found pores with a pore size of 1–10 μm in SiC whisker-reinforced AA, suggesting that these pores originate from cracks in AA in composite materials. For the majority of porous materials, their strength depends on the image composition and microstructure, especially the porosity [39]. The microstructure of AA is depicted in Figure 3e, f, where SEM (Figure 3e) shows that the alumina aerogel compounded by fiber is still a network porous structure formed by the accumulation of nanoparticles, and the TEM (Figure 3f) image displays that the 10–20 nm spherical Al-O-Al particles of AA form a three-dimensional network structure with a uniform mesoporous structure.
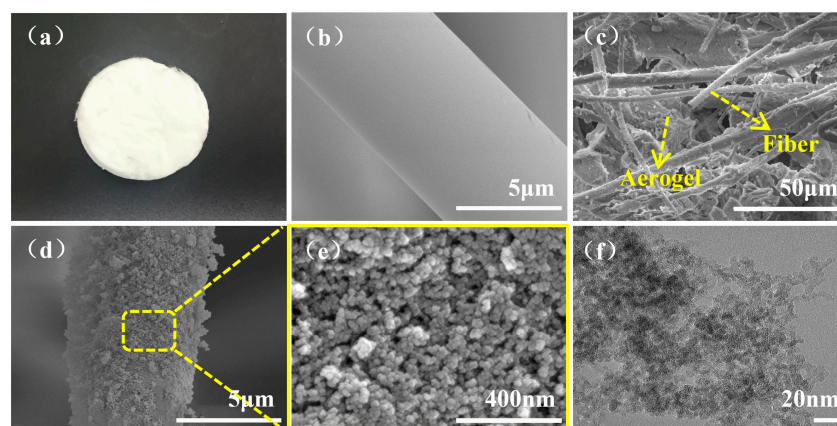

Figure 3. (**a**) Digital images of ASF/AA; (**b**) SEM images of ASF; (**c**) ASF/AA composite; (**d**) a single ASF is embedded in AA; (**e**) the SEM image; (**f**) TEM image of AA.

Figure 4a displays the XRD patterns of ASF/AA heated at various temperatures. A single broad diffraction peak at 23° was visible in the prepared ASF/AA. This peak originated from the composite's aluminum silicate fiber, which was amorphous at temperatures lower than 1000 °C. The diffraction peaks at 2θ = 28°, 38°, 49°, and 65° indicate that aerogel is boehmite (AlO(OH)), which is amorphous. The boehmite peak of the sample may be weakened by TEOS modification. After heat treatment at 600 °C and 800 °C, the AlO(OH) crystal phase disappeared, and the steamed bread peaked at 41° and 65°, indicating that a γ-Al$_2$O$_3$ crystal direction was formed [40]. This aligns with the findings of the TG-DSC (Figure 4d). During thermal processing at 1000 °C, the sample exhibited clear and prominent diffraction peaks and began to form the mullite phase (3Al$_2$O$_3$·2SiO$_2$) and α-Al$_2$O$_3$ phase. Because mullite has a high melting point, high thermal stability, and strong chemical stability, mullite phase development helps improve the properties of composite materials [41]. The sample's corresponding α-Al$_2$O$_3$ peak did not form after 1200 °C thermal processing; only the peak of the mullite phase was visible; this will also help the sample to maintain low thermal conductivity at high temperatures [42,43].
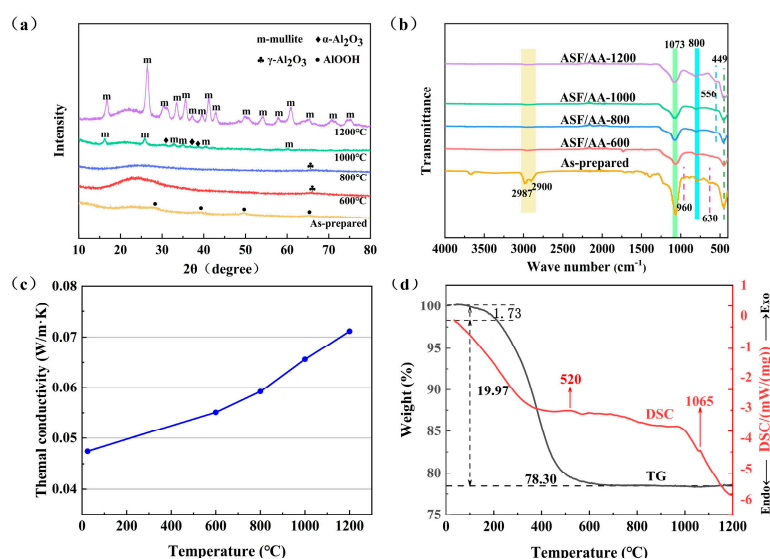

Figure 4. (**a**) XRD patterns and (**b**) FTIR spectra of ASF/AA thermal processing at different temperatures; (**c**) thermal conductivity of ASF/AA thermal processing at different temperatures; (**d**) TG-DSC curves of Al$_2$O$_3$ aerogel.

Following thermal processing at various temperatures, FTIR was utilized to investigate the ASF/AA composites further. The findings are displayed in Figure 4b. The samples without heat treatment correspond to the symmetric and antisymmetric tensile vibration peaks of -CH$_3$ at 2987 cm^{-1} and 2900 cm^{-1}, respectively. The peak mainly comes from Po, and as the temperature increases, Po gradually weakens and eventually disappears. The peak near 1073 cm^{-1} is the absorption peak of Al-O-Al, while the vibration absorption peaks of the tetrahedron Al-O are located near 449 cm^{-1} and 800 cm^{-1}. Nevertheless, due to the influence of residual metal elements (Si, Fe, Cr, etc.) in the treated aluminum silicate fibers and coal gangue, the position of the aluminum oxygen absorption peak has shifted. The unheated-treated samples showed significant combined vibration absorption peaks of Al-OH at 960 cm^{-1} and 630 cm^{-1}, corresponding to AlOOH [44]. After heat treatment at temperatures above 600 °C, the peak intensity weakens and eventually disappears. After treatment at temperatures above 800 °C, an Al-O-Al tensile vibration absorption peak appeared near 556 cm^{-1} [45], indicating the phase transition of the aerogel from AlOOH to other crystalline phases. The simultaneous appearance of shoulders on the high and low sides of the 1180 cm^{-1} absorption band indicates the presence of Si-O-Al bonds through the cross condensation of Al$_2$O$_3$ and SiO$_2$ [46]. After heat treatment at 1000 °C and 1200 °C,

the peak intensity becomes stronger, corresponding to the mullite crystal phase. At this stage, the Al-OH group disappears and the crystal structure is completely formed.

3.4. Thermal Stability Property

The heat-treated composite materials' high-temperature thermal resilience was examined by putting them through a variety of tests. The thermal conductivity of ASF/AA at 600, 800, 1000, and 1200 °C, both before and after heat treatment, is displayed in Figure 4c. As the temperature rises, so does the thermal conductivity. When the temperature increases, the thermal movement of solid molecules in ASF/AA is enhanced, while the heat conduction of air in the pores of the material and the radiation between the pore walls are also increased, especially at high temperatures. The thermal conductivity of ASF/AA is 0.047 W/(m·K) at room temperature and 0.071 W/(m·K) after treatment at 1200 °C, which indicates low thermal conductivity in fiber/aerogel composite insulation materials [47]. This can be explained by the microstructure (Figure 3c). The aerogels filled in the space between the fibers, making the composite obtain a mesoporous structure and effectively reducing the thermal conductivity. The TG-DSC curve of AA increased from ambient temperature to 1200 °C in an argon environment is displayed in Figure 4d. Between 20 °C and 1200 °C, the mass loss rate is 21.7%. There are three primary stages to the thermal imaging curve. The desorption of a tiny amount of physically adsorbed water and leftover organic matter is the primary cause of the weight loss of 1.73% that happens in the first stage between ambient temperature and 200 °C. In the second stage, 19.97% of weight loss occurs in the temperature range of 200 to 700 °C, and a broad endothermic peak appears at 520 °C. This is due to the oxidation of Po-derived CH_3 and the transition from boehmite crystals to γ-structural transformation of Al_2O_3 (2AlO (OH)) $\rightarrow$ γ-Al_2O_3 + H_2O, 300–980 °C) [48]. The third stage is 1000 °C to 1200 °C, during which there is almost no weight loss, and there is an exothermic peak at 1065 °C. The exothermic peak is prepared by the mullite phase transition ($3Al_2O_3$ + $2SiO_2$ $\rightarrow$ $3Al_2O_3 \cdot 2SiO_2$) at an elevated temperature [47,48]. In accordance with the TG-DSC curve, the accompanying XRD patterns also show that the mullite phase first appears at 1000 °C.

The SEM images of the ASF/AA composites at various temperatures following heat treatment are displayed in Figure 5a–d. The optical images demonstrate that after being calcined at various temperatures, the samples' morphology did not shrink or destruct. The SEM image of AA at 600 °C after heat treatment is shown in Figure 5a, where the aerogel particles are flat. The SEM picture of the aerogel treated at 800 °C is displayed in Figure 5b. At this time, the aerogel particles have more fragmentation and reaggregation phenomena, and the sheet structure appears. With the increase in pore size, the overall pore structure becomes loose, the pore size increases, and the corresponding specific surface area decreases [49]. After being treated at 1000 °C (Figure 5c), the pores in the figure are larger, the structure is further loosened, and the layered structure is more obvious. A large number of nanoparticles accumulate randomly to form relatively dense aggregates, and the appearance of new AA crystals will also produce a pore structure, the pore size distribution is not uniform, but still a mesoporous structure. At 1200 °C (Figure 5d), the particles become larger and denser, with a smooth appearance. This results from the mullite fossilization of SiO-Al particles [50]. Although another part of the pore structure is destroyed and collapsed, the microstructure of AA still appears as a porous structure [51].

Figure 6 displays the N_2 adsorption and desorption isotherms of BJH after heat treatment with AAs at different temperatures (Figure 6a) and the pore size distribution curve (Figure 6b). The isotherms of the composites treated at 600, 800, 1000, and 1200 °C are similar, all of which are type IV isotherms with H1 hysteresis curves. This is generally caused by typical capillary condensation occurring in mesopores [52]. This indicates that under high relative pressure (P/P_0 = 0.70–0.98), the sample still maintains the mesoporous structure characteristics of cylindrical holes after heat treatment at various temperatures. When the heat treatment temperature is 1200 °C, the area of the hysteresis ring on the adsorption–desorption isotherm decreases obviously, and the mesoporous structure of the

sample decreases obviously, which corresponds to the aperture distribution. According to the pore size distribution, the average pore size of the sample without heat treatment is 8.35 nm, and the pore size distribution is narrow. After heat treatment at 600 °C and 800 °C, the average pore diameter of the sample was 10.04 nm and 11.22 nm, respectively. Micropores disappeared and pore size distribution widened. This occurred 12.04 nm after heat treatment at 1000 °C and 13.54 nm after heat treatment at 1200 °C. The reason for this phenomenon is that due to the expansion and merger of AA particles and the merger and collapse of pores, new pores are formed, resulting in a larger average pore size. It is further proved that the samples are composed of mesoporous structures of different sizes. The pore size of 2–5 nm is formed by a large number of intergranular connections. The pore size of 10–50 nm is a nanoparticle formed by connecting clusters of the following components [53]. The prepared AA had a specific surface area of 608 m^2/g. The specific surface area attained under supercritical drying conditions is equal to that of AA. Hernandez et al., for instance, created AA via super-critical drying with a specific surface area of 662 m^2/g [54]. The specific surface area decreases as the particle size increases with temperature. The materials retain their mesoporous structure even after heat treatment at varying temperatures, with pore sizes ranging from 2 to 50 nm, while still retaining the mesoporous structure. Furthermore, this aperture is smaller than the typical free path of air molecules, which is 69 nm [55]. As a result, the prepared sample can effectively inhibit the generation of gas heat conduction and convection, and achieve a good thermal insulation effect.
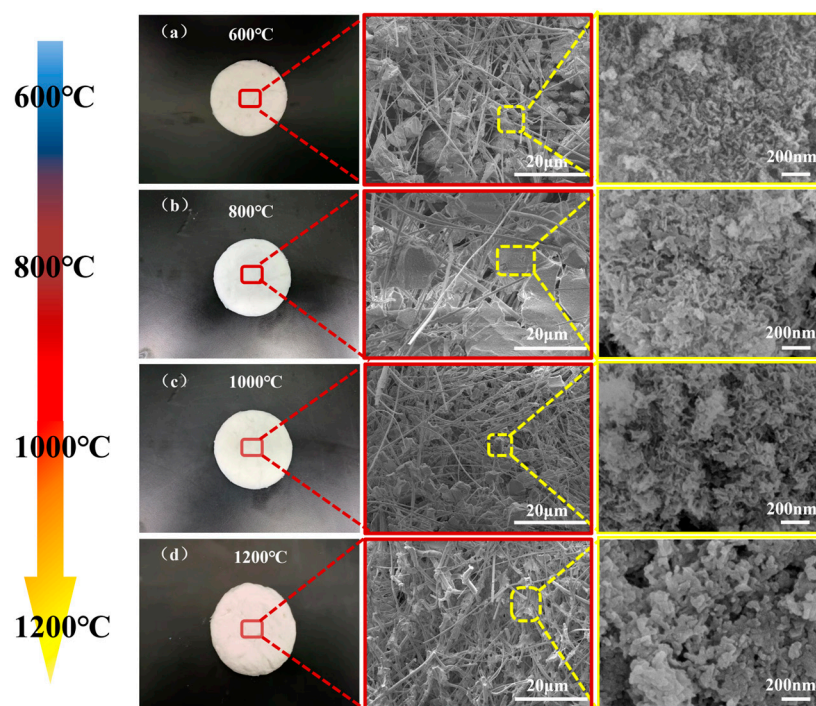

Figure 5. SEM images and optical pictures of ASF/AA composite at different temperatures: (**a**) ASF/AA-600; (**b**) ASF/AA-800; (**c**) ASF/AA-1000; (**d**) ASF/AA-1200.

As can be seen in Figure 7, ASF/AA and alumina aerogels have pore structures that are comparable to one another. Both composites correspond to type IV isotherms with H1 hysteresis curves, demonstrating that they are also mesoporous materials. The composite has a specific surface area of 416 m^2/g, which is less than that of pure alumina aerogel. The composite has bigger pores than pure alumina aerogel, with a concentrated range of 20–50 nm in size. This demonstrates that the aerogel's pore structure was unaffected by the addition of fibers.
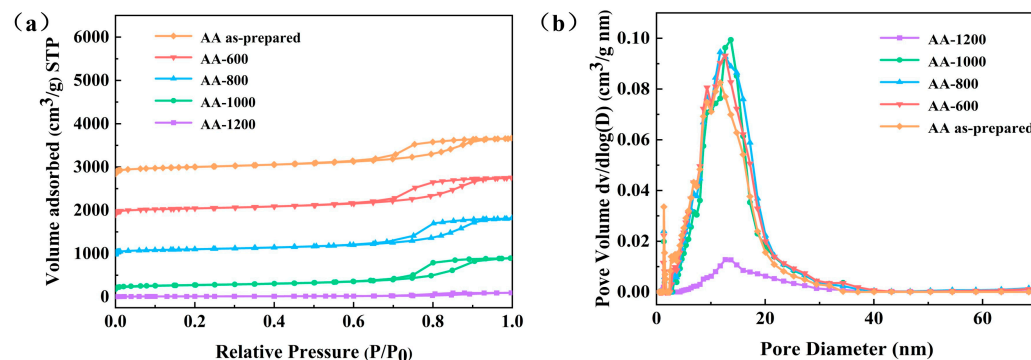
Figure 6. (**a**) N_2 adsorption–desorption isotherms; (**b**) pore size distribution curve.
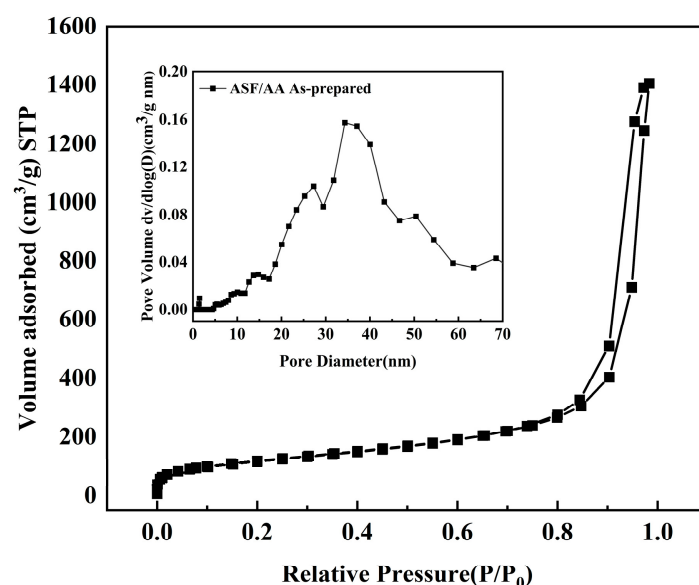

Figure 7. Pore structure analysis of the ASF/AA.

In an air environment, a single side of ASF/AA was heated with a butane spray gun (1200 °C for 20 min with a sample thickness of 10 mm (Figure 8c)). As shown in Figure 8a,b, no macroscopic damage occurred before and after heating of the sample, but a certain shrinkage occurred. At the end of the experiment, there was a gap between the aerogels and fibers on the hot and cold face (Figure 8d,g), and the aerogels (slightly contracted) still maintained their leaf-like morphology and mesoporous structure (Figure 8e,h). The hot and cold sides of the sample were measured via XRD and FTIR. The results of XRD (Figure 8f) show that the mullite phase diffraction peak appears on the hot side and the AlOOH diffraction peak appears on the cold side. As shown in Figure 8i, the absorption peak of Al-O-Si appeared on the hot side of the sample, and the mullite phase was formed on the hot side.

As shown in Figure 8j–l, ASF/AA with a thickness of 10 mm exhibits a thermal insulation effect on high temperatures, creating a huge temperature difference on both sides of the sample. The temperature on the side that is not directly heated is only 50 °C. Taken together, the results show that the sample has good thermal insulation performance and can effectively isolate heat at high temperatures. The prepared ASF/AA has the potential to be an ideal insulating material at temperatures up to 1200 °C.
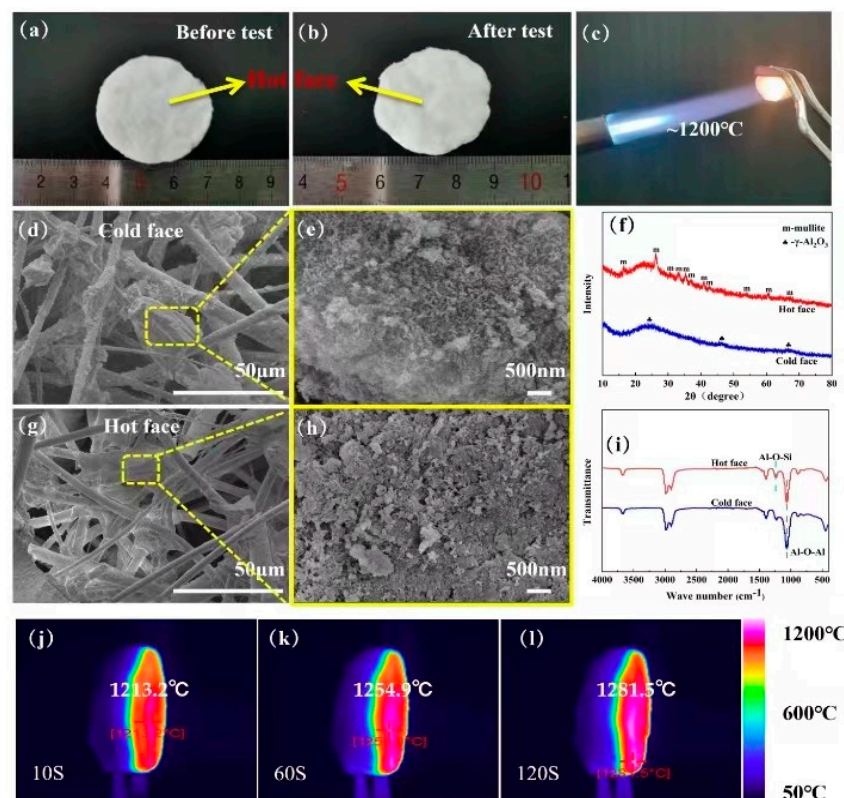
Figure 8. ASF/AA butane burner single side heating test: (**a**,**b**) appearance pictures before and after the test; (**c**) experiment images; (**d**) the microstructure of samples (**e**,**g**,**h**); (**f**) the XRD pattern of the sample (m: mullite; ♣: γ-Al$_2$O$_3$) and (**i**) FTIR spectra of samples; (**j**–**l**) the prepared ASF/AA burned with a butane spray gun for 10 s, 60 s, and 120 s in infrared images.

4. Conclusions

The ASF/AA aerogel composite material was synthesized via sol-gel, TEOS modification, and APD using CG as the aluminum source. The maximum aluminum-extraction rate was obtained by studying the factors affecting the calcination temperature, holding time, and the mass ratio of acid waste. The composites were characterized via XRD, FTIR, BET, TG-DSC, SEM, and TEM. The conclusions are as follows.

(1) The calcination temperature is 800 °C, the holding time is 0.5 h, and the mass ratio of acid waste is 0.96:1. Under this condition, most of the Al$_2$O$_3$ in CG can be extracted, and the extraction rate reaches 81.02%.

(2) The final prepared ASF/AA has similar low density (0.26 g/cm^3) and low thermal conductivity (0.047 W/(m·K)) at room temperature compared to the supercritical dried fiber/aerogel material.

(3) ASF/AA has good high-temperature resistance. After two hours of heat treatment at 1200 °C, the thermal conductivity stayed low (0.071 W/(m·K)). The composite's high-temperature thermal stability is enhanced by the mullite phase that forms after heat treatment above 1000 °C. The infrared imaging pictures show that the composite material has a strong ability to insulate against heat.

In conclusion, our research provides a method for realizing the high-value utilization of CG solid waste and the synthesis of low-cost, high-performance thermal insulation materials. The composite materials have certain potential application value in industry, building materials, aerospace, and other fields.

References

1. Li, J.; Wang, J. Comprehensive utilization and environmental risks of coal gangue: A review. *J. Clean. Prod.* **2019**, *239*, 117946. [CrossRef]
2. Liang, Y.C.; Liang, H.D.; Zhu, S.Q. Mercury emission from spontaneously ignited coal gangue hill in Wuda coalfield, Inner Mongolia, China. *Fuel* **2016**, *182*, 525–530. [CrossRef]
3. Li, Q.; Lv, L.; Zhao, X.; Wang, Y.; Wang, Y. Cost-effective microwave-assisted hydrothermal rapid synthesis of analcime-activated carbon composite from coal gangue used for Pb^{2+} adsorption. *Environ. Sci. Pollut. Res.* **2022**, *29*, 77788–77799. [CrossRef] [PubMed]
4. Li, X.; Wang, H.; Zhou, Q.; Qi, T.; Liu, G.; Peng, Z. Efficient separation of silica and alumina in simulated CFB slag by reduction roasting-alkaline leaching process. *Waste Manag.* **2019**, *87*, 798–804. [CrossRef] [PubMed]
5. Zhao, N.; Zhang, Y.; Zhao, X.; Yang, N.; Wang, Z.; Guo, Z.; Tong, J.; Zhang, Y.; Liu, Z. Temperature Distribution Regularity and Dynamic Evolution of Spontaneous Combustion Coal Gangue Dump: Case Study of Yinying Coal Mine in Shanxi, China. *Sustainability* **2023**, *15*, 6362. [CrossRef]
6. Li, L.; Long, G.; Bai, C.; Ma, K.; Wang, M.; Zhang, S. Utilization of Coal Gangue Aggregate for Railway Roadbed Construction in Practice. *Sustainability* **2020**, *12*, 4583. [CrossRef]
7. Li, Y.; Yao, Y.; Liu, X.; Sun, H.; Ni, W. Improvement on pozzolanic reactivity of coal gangue by integrated thermal and chemical activation. *Fuel* **2013**, *109*, 527–533. [CrossRef]
8. Peng, Z.; Liu, Z.; Gao, Y.; Liu, J.; Wang, D.; Liu, H.; Zhang, Y.; Li, L. Synthesis and CO_2 adsorption performance of high Si/Al ratio DDR zeolites prepared from silica fume. *J. Environ. Chem. Eng.* **2023**, *11*, 110837. [CrossRef]
9. Xiong, J.; Zang, L.; Zha, J.; Mahmood, Q.; He, Z. Phosphate Removal from Secondary Effluents Using Coal Gangue Loaded with Zirconium Oxide. *Sustainability* **2019**, *11*, 2453. [CrossRef]
10. Cai, H.; Jiang, Y.; Chen, Q.; Zhang, S.; Li, L.; Feng, J.; Feng, J. Sintering behavior of SiO_2 aerogel composites reinforced by mullite fibers via in-situ rapid heating TEM observations. *J. Eur. Ceram. Soc.* **2020**, *40*, 127–135. [CrossRef]
11. Koebel, M.; Rigacci, A.; Achard, P. Aerogel-based thermal superinsulation: An overview. *J. Sol-Gel Sci. Technol.* **2012**, *63*, 315–339. [CrossRef]
12. Lamy-Mendes, A.; Pontinha, A.D.R.; Alves, P.; Santos, P.; Durães, L. Progress in silica aerogel-containing materials for buildings' thermal insulation. *Constr. Build. Mater.* **2021**, *286*, 122815. [CrossRef]
13. Xie, F.; Dai, X.; Zhuo, L.; Dai, Q.; He, C.; Lu, Z. Robust BNNS/ANF aerogel skeleton-based PEG composite phase change materials with high latent heat for efficient thermal management. *Compos. Struct.* **2023**, *323*, 117479. [CrossRef]
14. Kotov, E.V.; Nemova, D.; Sergeev, V.; Dontsova, A.; Koriakovtseva, T.; Andreeva, D. Thermal Performance Assessment of Aerogel Application in Additive Construction of Energy-Efficient Buildings. *Sustainability* **2024**, *16*, 2398. [CrossRef]
15. Baumann, T.F.; Kucheyev, S.O.; Gash, A.E.; Satcher, J.H. Facile synthesis of a cryHstalline, high-surface-area SnO_2 aerogel. *Adv. Mater.* **2005**, *17*, 1546–1548. [CrossRef]
16. Tokudome, Y.; Nakanishi, K.; Kanamori, K.; Fujita, K.; Akamatsu, H.; Hanada, T. Structural characterization of hierarchically porous alumina aerogel and xerogel monoliths. *J. Colloid. Interf. Sci.* **2009**, *338*, 506–513. [CrossRef]
17. Bao, B.Y.; Wang, I.; Haines, T.; Ren, L.; Tian, H.; Hu, J. Methane decomposition for the production of COx-free hydrogen and carbon nanotubes over transition metal aerogel catalysts. *Abstr. Pap. Am. Chem. Soc.* **2018**, *256*.
18. Gao, B.; Yuan, G.; Ren, L. Polydiacetylene-functionalized alumina aerogels as visually observable sensing materials for detecting VOCs concentration. *J. Mater. Sci.* **2018**, *53*, 6698–6706. [CrossRef]
19. Hurwitz, F.I.; Gallagher, M.; Olin, T.C.; Shave, M.K.; Ittes, M.A.; Olafson, K.N.; Fields, M.G.; Rogers, R.B.; Guo, H.Q. Optimization of Alumina and Aluminosilicate Aerogel Structure for High-Temperature Performance. *Int. J. Appl. Glass Sci.* **2014**, *5*, 276–286. [CrossRef]
20. Hayase, G.; Nonomura, K.; Hasegawa, G.; Kanamori, K.; Nakanishi, K. Ultralow-Density, Transparent, Superamphiphobic Boehmite Nanofiber Aerogels and Their Alumina Derivatives. *Chem. Mater.* **2015**, *27*, 3–5. [CrossRef]

21. Zhang, Z.; Scherer, G.W. Supercritical drying of cementitious materials. *Cem. Concr. Res.* **2017**, *99*, 137–154. [CrossRef]
22. Liu, F.; Jiang, Y.; Peng, F.; Feng, J.; Li, L.; Feng, J. Fiber-reinforced alumina-carbon core-shell aerogel composite with heat-induced gradient structure for thermal protection up to 1800 °C. *Chem. Eng. J.* **2023**, *461*, 141721. [CrossRef]
23. Wang, H.; Quan, X.; Yin, L.; Jin, X.; Pan, Y.; Wu, C.; Huang, H.; Hong, C.; Zhang, X. Lightweight quartz fiber fabric reinforced phenolic aerogel with surface densified and graded structure for high temperature thermal protection. *Compos. Part. A Appl. Sci. Manuf.* **2022**, *159*, 107022. [CrossRef]
24. Yang, X.; Wei, J.; Shi, D.; Sun, Y.; Lv, S.; Feng, J.; Jiang, Y. Comparative investigation of creep behavior of ceramic fiber-reinforced alumina and silica aerogel. *Mater. Sci. Eng. A* **2014**, *609*, 125–130. [CrossRef]
25. Kim, C.-Y.; Lee, J.-K.; Kim, B.-I. Synthesis and pore analysis of aerogel-glass fiber composites by ambient drying method. *Colloid. Surf. A* **2008**, *313*, 179–182. [CrossRef]
26. Zhang, R.; Hou, X.; Ye, C.; Wang, B. Enhanced mechanical and thermal properties of anisotropic fibrous porous mullite-zirconia composites produced using sol-gel impregnation. *J. Alloys Compd.* **2017**, *699*, 511–516. [CrossRef]
27. Zhu, Z.; Wang, F.; Yao, H.; Dong, J.; Long, D. High-temperature Insulation Property of Opacifier-doped Al_2O_3-SiO_2 Aerogel/Mullite Fiber Composites. *J. Inorg. Mater.* **2018**, *33*, 969–975.
28. Du, D.; Sun, L.; Sun, C.; Liu, Z.; Guo, X.; Zhang, Y. Synthesis of alumina aerogel enriched carboxymethyl cellulose with polymodal pore size distribution by ambient pressure drying. *Cellulose* **2023**, *30*, 11369–11385. [CrossRef]
29. Han, Y.; Wu, Y.; Huang, S.; Zhang, H.; Liang, Z.; Guan, X.; Wu, S. Convenient and rapid preparation of aerogels dried at ambient pressure. *J. Non-Cryst. Solids* **2023**, *622*, 122665. [CrossRef]
30. Shewale, P.M.; Rao, A.V.; Rao, A.P. Effect of different trimethyl silylating agents on the hydrophobic and physical properties of silica aerogels. *Appl. Surf. Sci.* **2008**, *254*, 6902–6907. [CrossRef]
31. Zhang, H.; Fang, W.-Z.; Wang, X.; Li, Y.-M.; Tao, W.-Q. Thermal conductivity of fiber and opacifier loaded silica aerogel composite. *Int. J. Heat. Mass. Tran.* **2017**, *115*, 21–31. [CrossRef]
32. Karlina, A.I.; Karlina, Y.I.; Gladkikh, V.A. Analysis of Experience in the Use of Micro- and Nanoadditives from Silicon Production Waste in Concrete Technologies. *Minerals* **2023**, *13*, 1525. [CrossRef]
33. Liu, F.; Xie, M.; Yu, G.; Ke, C.; Zhao, H. Study on Calcination Catalysis and the Desilication Mechanism for Coal Gangue. *ACS Sustain. Chem. Eng.* **2021**, *9*, 10318–10325. [CrossRef]
34. Wang, H.; Zhang, X.; Liu, C.; Shen, L. Comprehensive Extraction of Silica and Alumina from High-Alumina Coal Gangue (HACG): Hematite Involved Roasting—Alkaline Leaching—Bayer Digestion Process. *J. Sustain. Metall.* **2021**, *7*, 1686–1698. [CrossRef]
35. Zhang, T.; Yang, H.; Zhang, H.; Zhang, P.; Bei, R. Aluminum extraction from activated coal gangue with carbide slag. *J. Anal. Appl. Pyrolysis* **2022**, *163*, 105504. [CrossRef]
36. Xiao, J.; Li, F.; Zhong, Q.; Bao, H.; Wang, B.; Huang, J.; Zhang, Y. Separation of aluminum and silica from coal gangue by elevated temperature acid leaching for the preparation of alumina and SiC. *Hydrometallurgy* **2015**, *155*, 118–124. [CrossRef]
37. Peng, F.; Jiang, Y.; Feng, J.; Cai, H.; Feng, J.; Li, L. Thermally insulating, fiber-reinforced alumina-silica aerogel composites with ultra-low shrinkage up to 1500 °C. *Chem. Eng. J.* **2021**, *411*, 128402. [CrossRef]
38. Mizushima, Y.; Hori, M. Preparation of heat-resistant alumina aerogels. *J. Mater. Res.* **1993**, *8*, 2993–2999. [CrossRef]
39. Zou, W.; Wang, X.; Wu, Y.; Zu, G.; Zou, L.; Zhang, R.; Yao, X.; Shen, J. Highly thermally stable alumina-based aerogels modified by partially hydrolyzed aluminum tri-sec-butoxide. *J. Sol-Gel Sci. Technol.* **2017**, *84*, 507–514. [CrossRef]
40. Wu, X.; Shao, G.; Cui, S.; Wang, L.; Shen, X. Synthesis of a novel Al_2O_3-SiO_2 composite aerogel with high specific surface area at elevated temperatures using inexpensive inorganic salt of aluminum. *Ceram. Int.* **2016**, *42*, 874–882. [CrossRef]
41. Peng, F.; Jiang, Y.; Feng, J.; Feng, J.; Li, L. Foreign element doping and thermal stability of alumina aerogels. *J. Am. Ceram. Soc.* **2022**, *105*, 2288–2299. [CrossRef]
42. Wu, Z.-G.; Zhao, Y.-X.; Liu, D.-S. The synthesis and characterization of mesoporous silica–zirconia aerogels. *Microporous Mesoporous Mater.* **2004**, *68*, 127–132. [CrossRef]
43. Li, D.-Y.; Lin, Y.-S.; Li, Y.-C.; Shieh, D.-L.; Lin, J.-L. Synthesis of mesoporous pseudoboehmite and alumina templated with 1-hexadecyl-2,3-dimethyl-imidazolium chloride. *Microporous Mesoporous Mater.* **2008**, *108*, 276–282. [CrossRef]
44. Ren, T.-Z.; Yuan, Z.-Y.; Su, B.-L. Microwave-Assisted Preparation of Hierarchical Mesoporous−Macroporous Boehmite AlOOH and γ-Al_2O_3. *Langmuir* **2004**, *20*, 1531–1534. [CrossRef] [PubMed]
45. Aravind, P.R.; Mukundan, P.; Krishna Pillai, P.; Warrier, K.G.K. Mesoporous silica–alumina aerogels with high thermal pore stability through hybrid sol–gel route followed by subcritical drying. *Microporous Mesoporous Mater.* **2006**, *96*, 14–20. [CrossRef]
46. Xing, B.-L.; Guo, H.; Chen, L.-J.; Chen, Z.-F.; Zhang, C.-X.; Huang, G.-X.; Xie, W.; Yu, J.-L. Lignite-derived high surface area mesoporous activated carbons for electrochemical capacitors. *Fuel Process. Technol.* **2015**, *138*, 734–742. [CrossRef]
47. Wu, X.; Shao, G.; Shen, X.; Cui, S.; Wang, L. Novel Al_2O_3–SiO_2 composite aerogels with high specific surface area at elevated temperatures with different alumina/silica molar ratios prepared by a non-alkoxide sol-gel method. *RSC Adv.* **2016**, *6*, 5611–5620. [CrossRef]
48. Aripin, H.; Mitsudo, S.; Prima, E.S.; Sudiana, I.N.; Kikuchi, H.; Sano, S.; Sabchevski, S. Crystalline mullite formation from mixtures of alumina and a novel material—Silica xerogel converted from sago waste ash. *Ceram. Int.* **2015**, *41*, 6488–6497. [CrossRef]
49. Li, J.-Y.; Tian, B.-H.; Li, X.-X.; Wang, Z.; Cui, L.-P.; Liang, D.-D.; Wang, S.-L.; Liu, Y.-H.; Ou, H.-A.; Liang, H.-X. Energy effective utilization of circulating fluidized bed fly ash to prepare silicon-aluminum composite aerogel and gypsum. *Waste Manag.* **2023**, *172*, 162–170. [CrossRef]

50. Yi, Z.; Zhang, X.; Yan, L.; Huyan, X.; Zhang, T.; Liu, S.; Guo, A.; Liu, J.; Hou, F. Super-insulated, flexible, and high resilient mullite fiber reinforced silica aerogel composites by interfacial modification with nanoscale mullite whisker. *Compos. Part. B Eng.* **2022**, *230*, 109549. [CrossRef]

51. Liu, Z.-H.; Ding, Y.-D.; Wang, F.; Deng, Z.-P. Thermal insulation material based on SiO$_2$ aerogel. *Constr. Build. Mater.* **2016**, *122*, 548–555. [CrossRef]

52. Hench, L.L.; West, J.K. The sol-gel process. *Chem. Rev.* **1990**, *90*, 33–72. [CrossRef]

53. Gao, M.; Liu, B.; Zhao, P.; Yi, X.; Shen, X.; Xu, Y. Mechanical strengths and thermal properties of titania-doped alumina aerogels and the application as high-temperature thermal insulator. *J. Sol-Gel Sci. Technol.* **2019**, *91*, 514–522. [CrossRef]

54. Hernandez, C.; Pierre, A.C. Evolution of the Texture and Structure of SiO$_2$–Al$_2$O$_3$ Xerogels and Aerogels as a Function of the Si to Al Molar Ratio. *J. Sol-Gel Sci. Technol.* **2001**, *20*, 227–243. [CrossRef]

55. Zhang, E.; Zhang, W.; Lv, T.; Li, J.; Dai, J.; Zhang, F.; Zhao, Y.; Yang, J.; Li, W.; Zhang, H. Insulating and Robust Ceramic Nanorod Aerogels with High-Temperature Resistance over 1400 °C. *ACS Appl. Mater. Interfaces* **2021**, *13*, 20548–20558. [CrossRef]